Materials Science and Engineering C 29 (2009) 1467–1479

Contents lists available at ScienceDirect

Materials Science and Engineering C

journal homepage: www.elsevier.com/locate/msec

LHRH-functionalized superparamagnetic iron oxide nanoparticles for breast cancer targeting and contrast enhancement in MRI

J. Meng [a], J. Fan [a], G. Galiana [b], R.T. Branca [c], P.L. Clasen [d], S. Ma [d], J. Zhou [a], C. Leuschner [e,*], C.S.S.R. Kumar [f], J. Hormes [f], T. Otiti [g], A.C. Beye [h], M.P. Harmer [d], C.J. Kiely [d], W. Warren [c,*], M.P. Haataja [a], W.O. Soboyejo [a,*]

[a] Princeton Institute of Science and Technology of Materials and the Department of Mechanical and Aerospace Engineering, Princeton University, Princeton, NJ 08544, United States
[b] Department of Chemistry, Princeton University, Princeton, NJ 08544, United States
[c] Department of Chemistry, Duke University, Durham, NC 27708-0354, United States
[d] Center for Advanced Materials and Nanotechnology, Lehigh University, Bethlehem, PA 18015-3195, United States
[e] Pennington Biomedical Research Center, 6400 Perkins Road, Baton Rouge, LA 70808, United States
[f] Center for Advanced Microstructures and Devices, Louisiana State University, 6980 Jefferson Hwy, Baton Rouge, LA 70806, United States
[g] Department of Physics, Makerere University, Kampala, Uganda
[h] Department of Physics, Cheikh Anta Diop University, Dakar, Senegal

ARTICLE INFO

Article history:
Received 10 March 2008
Received in revised form 4 September 2008
Accepted 15 September 2008
Available online 7 October 2008

Keywords:
Magnetic nanoparticles
Breast cancer detection
Receptor-mediated endocytosis

ABSTRACT

This paper shows that superparamagnetic iron oxide nanoparticles (SPIONs) conjugated to luteinizing hormone releasing hormone (LHRH) (LHRH–SPIONs), can be used to target breast cancer cells. They also act as contrast enhancement agents during the magnetic resonance imaging of breast cancer xenografts. A combination of transmission electron microscopy (TEM) and spectrophotometric analysis was used in our experiments, to investigate the specific accumulation of the functionalized superparamagnetic iron oxide nanoparticles (SPIONs) in cancer cells. The contrast enhancement of conventional T2 images obtained from the tumor tissue and of breast cancer xenograft bearing mice is shown to be much greater than that in saline controls, when the tissues were injected with LHRH–SPIONs. Magnetic anisotropy multi-CRAZED images of tissues extracted from mice injected with SPIONs were also found to have enhanced MRI contrast in breast cancer xenografts and metastases in the lungs.

1. Introduction

In the United States, breast cancer is the second leading cause of cancer death in women. In 2005, 40,410 deaths were attributed to breast cancer in the United States alone [1]. In the absence of a cure, the real clinical challenge is early detection. However, the early detection of breast cancer is limited by the spatial resolution of the methods that are currently used to detect cancer.

In the case of magnetic resonance imaging (MRI), the current spatial resolution of detection is of the order of a few millimeters [2]. This corresponds to hundreds of millions of cancer cells, and therefore a greater probability of it being a later stage of cancer. There is, however, a need to further develop imaging methods that can enhance the contrast and spatial resolution of tumor tissue in MRI.

Gadolinium based contrast agents have been used in MRI over the past few decades [3,4]. These do provide enhanced contrast that can overcome tissue heterogeneity, but the spatial resolution provided by gadolinium contrast agents is still limited to a few millimeters. Furthermore, the attachment of current gadolinium contrast agents is not specific, *i.e.* they do not have ligands that bind specifically to tumor sites.

Besides gadolinium ion complexes, MRI contrast agents based on superparamagnetic iron oxide nanoparticles (SPIONs) are also commercially available (See Table 1). Dextran coated iron oxides are biocompatible and are selectively taken up by the reticuloendothelial system, a network of cells lining blood vessels whose function is to remove foreign substances from the blood system. These SPIONs accumulate in the liver and are later excreted via the liver after treatment. Hence, they can specifically enhance the MRI contrast of liver tissue [5].

Smaller iron oxide nanoparticles with sizes of ~10 nm have a longer half-time in the blood stream and are collected by reticulo-endothelial cells, which are also distributed in lymph nodes and bone marrow [6]. However, since tumor cells do not have reticuloendothelial systems, their relaxation times are not affected by such contrast agents. Nevertheless, these small nanoparticles have already been used to identify malignant lymph nodes [7], liver tumors [8] and brain tumors [9]. However there is still a definite need to develop ligand-bound magnetic nanoparticles that can attach specifically to other tumors.

Ligand conjugated superparamagnetic iron oxide nanoparticles (SPIONs) offer an alternative that can be used to overcome some of the

* Corresponding authors.
E-mail address: soboyejo@princeton.edu (W.O. Soboyejo).

0928-4931/$ – see front matter © 2008 Published by Elsevier B.V.
doi:10.1016/j.msec.2008.09.039

Table 1
Commercially available SPIONs for MRI contrast enhancement and their specific indication place.

Name of drug	Indication in MRI
Feridex®	Liver
Endorem™	Liver
GastroMARK®	Bowel marking
Lumirem®	Bowel marking
Sinerem®	MR angiography vascular, staging of RES-directed liver diseases, lymph nodes
Resovist®	Liver lesions

http://www.mr-tip.com/.

limitations of existing gadolinium and SPION contrast agents. First, the attachment of specific ligands to such nanoparticles offers the potential for the design of systems that can target specific tumors [10]. In the case of breast cancer, prior work has shown that luteinizing hormone releasing hormone (LHRH) receptors are over-expressed on breast cancer cell membranes [11]. This stimulated Kumar et al. [11,12] and Leuschner et al. [11–16] to design superparamagnetic iron oxide nanoparticles conjugated to LHRH that can be used to target breast tumor sites. Hence, these entities have potential applications in cancer drug delivery and cancer diagnosis [17,18]. These highly specifically functionalized nanoparticles are often referred to as LHRH–SPIONs.

Transmission electron microscopy studies by Zhou et al. [19] later showed that the LHRH–SPIONs accumulate specifically in breast cancer xenografts *in-vivo*. Shannon et al. [20] have also conducted multi-CRAZED MRI experiments on the same breast cancer xenografts that were used in the TEM experiments of Zhou et al. [19]. The resulting MRI of tumor tissue samples showed that contrast enhanced in female mice breast tumor tissue injected with LHRH-conjugated superparamagnetic iron oxide nanoparticles (LHRH–SPIONs). However, there have been no prior reports of nanoparticle enhanced T2 MRI images of LHRH–SPIONs-containing breast tumors. There have also been relatively few *in-vitro* experiments designed to provide controlled insights into the time-dependent uptake of such nanoparticles.

This paper presents the results of systematic *in-vitro* and *in-vivo* experiments designed to quantify the uptake of unconjugated and LHRH-conjugated magnetite nanoparticles by breast cancer cells. It also extends the work by Shannon et al. [20] by comparing new multi-CRAZED images with T2 images of female mouse breast tumor tissue injected with LHRH-conjugated superparamagnetic iron oxide nanoparticles (LHRH–SPIONs). The intracellular LHRH–SPIONs provide significant contrast enhancement in conventional T2 images of breast cancer xenografts and in bulk T2 measurements. Enhanced MRI contrast is also shown to be provided by multi-CRAZED MRI images of the breast cancer xenografts and their metastases in the lungs. Finally, the possible implications of these results are discussed for the early detection and treatment of breast cancer.

2. Multi-Crazed MRI

In conventional magnetic resonance imaging, spin echoes are analyzed to determine relaxation times. Even 20 years ago, it was possible to calculate the effect of thousands of pulse sequences [21]. However, it was found that certain simple pulse sequences, which should theoretically give no signal, experimentally give strong peaks with a signal size 10% of the macroscopic magnetization, but 1000 times larger than the background noise. This conflict between theory and experiment leads to what are called "CRAZED" sequences [22]. At this time, it has been clearly established that this effect is related to the dipolar interactions between distant spins in solution [23].

The CRAZED sequences are in the form of: 90°-delay τ — Gradient Pulse, area GT — θ — Gradient Pulse, area nGT-delay, TE — 180°-delay (TE — $n\tau$), acquisition, as shown in Fig. 1 [20]. This produces signals from intermolecular n-quantum coherences involving spins separated by a "correlation distance," $d_C = \pi/(\gamma GT)$, where γ is the gyromagnetic ratio, and GT is the gradient pulse area. The contrast mechanism of the iMQC signal is based on the intrinsic sensitivity to magnetization and the susceptibility structure over a sub-voxel distance, which is different from conventional contrast.

As shown in Fig. 1, by adding new gradient pulses, an arbitrary number of echoes of different coherence orders can be acquired simultaneously. The ratio of the first two correlation gradients is 1:2, so the first acquisition window gives a +2-quantum image (DQC image). Subsequent echoes that are separated by a period τ can be acquired, as shown in Fig. 1. The associated correlation gradients provide +1-quantum imaging (SQC image), 0-quantum imaging (ZQC image), −1-quantum imaging (MSQC image), and −2-quantum imaging (MDQC image). The signals for a multi-CRAZED sequence can be expressed as introduced in Ref. [20].

3. Experimental procedures

3.1. Materials preparation

Five different kinds of SPION types were used in our experiments. The 15 nm SPIONs and 15 nm LHRH–SPIONs were prepared using the method described by Kumar et al. [12]. In order to prepare 15 nm SPIONs, 1.622 g of $FeCl_3$ and 0.994 g of $FeCl_2 \cdot 4H_2O$ were placed in a three-necked flask which was evacuated and flushed with nitrogen three times to remove oxygen. The iron salts were dissolved with stirring in 25 ml of water, and then 2.5 ml of 28% NH_4OH solution was added dropwise to this solution at room temperature. A black precipitate was obtained, which was heated at 80 °C for 30 min, washed several times with water followed by ethanol, and then finally dried in a vacuum oven at 70 °C. To prepare LHRH–SPIONS, 60 mg of 15 nm SPIONs were dispersed in 6 ml of water by sonication under nitrogen. A freshly prepared carbodiimide solution (42 mg in 1.5 ml of water) was added, and the solution was sonicated for a further 10 min. The mixture was then cooled to 4 °C before adding a solution of LHRH (3.7 mg in 1.5 ml of water). The reaction temperature was then maintained at 4 °C for 2 h, with occasional swirling of the flask. After 2 h, the flask was placed on a permanent magnet, and the nanoparticles were allowed to settle.

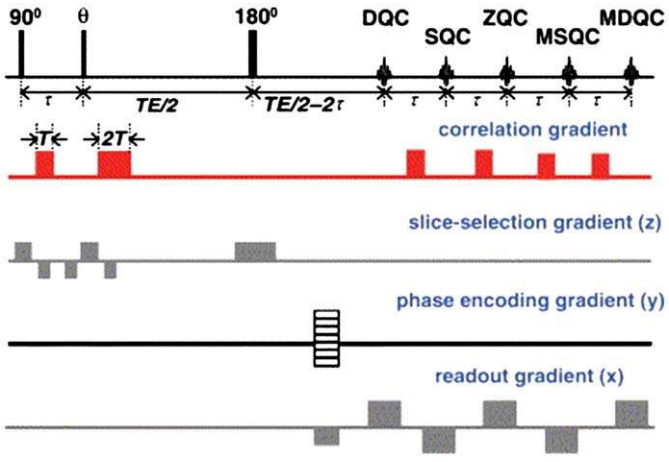

Fig. 1. Multi-CRAZED sequence to acquire multiple echoes. The multi-CRAZED sequence takes advantage of the difference in echo timing to acquire multiple echoes at full intensity. The +SQC (+1 or single-quantum coherence) and MSQC (−1 or single-quantum coherence) images have primarily conventional contrast; the DQC (+2-quantum), ZQC (0-quantum), and MDQC (−2-quantum) coherences have contrast from subvoxel variations in magnetization density or resonance frequency. Additional gradient pulses permit image acquisition in the standard way (single-line acquisition shown here) (adapted from Ref. [20]).

The 5 nm and 10 nm SPION solutions were synthesized from the thermal decomposition of iron carbonyl in the presence of oleic acid [24,25]. In order to prepare 5 nm and 10 nm particles, 1.062 g iron (III) acetylacetonate and 3.952 g 1,2-hexadecanediol were mixed in the presence of 2.85 ml oleic acid, 4.05 ml oleylamine and 30 ml diphenyl ether under argon flow. To produce 10 nm nanoparticles, the mixture was heated to 215 °C at a rate of 10 °C/min. It was then kept at 215 °C for 2 h. To produce 5 nm nanoparticles, the mixture was heated to 200 °C at a rate of 10 °C/min and was kept at 200 °C for 30 min. In both cases the mixture was subsequently refluxed at 265 °C for 30 min and then cooled to room temperature. Once cooling, the nanoparticle solution was precipitated by the addition of 60 ml ethanol and washed by centrifuge to remove the excess surfactant. The particles were then re-dispersed in 20 ml hexane with 100 μl oleic acid and 100 μl oleylamine.

The Fe_3O_4 nanoparticles were changed from a hydrophobic to hydrophilic character by the addition of a bipolar surfactant (tetramethylammonium-11-aminoundecanoate in dichloromethane) which facilitated an aqueous dispersion [24].

The 30 nm SPIONs were purchased directly from Aldrich-Sigma (St. Louis, MO 63178).

3.2. Characterization of nanoparticles

Transmission electron microscopy (TEM) was used to characterize the five different nanoparticle types and determine their size distributions. In order to prepare TEM specimens, the nanoparticles were dispersed in deionized water under sonication for 30 min. One droplet of the solution was then transferred onto continuous carbon film supported on a 300 mesh copper TEM grid. The 5 nm and 10 nm SPION solutions were dried at 50 °C on TEM grids tilted to a 60° which facilitated their self assembly in to well ordered nanoparticle arrays. The other TEM grids were dried in air at room temperature for one day, during which time the water to fully evaporate. The specimens were then observed in a LEO 912AB TEM (Zeiss, Thornwood, NY). Micrographs of the nanoparticle materials were then analyzed using Adobe Photoshop (Adobe, San Jose, CA) software in order to determine their respective particle size distributions.

3.3. In-vitro experiments

In-vitro experiments were used to study how the particle size and LHRH coating on magnetite nanoparticles affect their uptake into breast cancer cells. Both SPIONs and LHRH–SPIONs were suspended in a cell culture medium by sonicating them for 1 h. The concentration of different kinds of nanoparticle solution was controlled to be the same, *i.e.* 0.04 mg/ml in the TEM experiments and 0.005 mg/ml in the spectrophotometry experiments. Human breast cancer cells Hs 578T (HTB 126 from ATCC, American Type Culture Collection, Manassas, VA 20108) were cultured separately in these different media for different time periods. The cells were then used for transmission electron microscopy (TEM) and spectrophotometric studies of nanoparticle uptake.

3.3.1. Transmission electron microscopy

Transmission electron microscopy (TEM) was used to study the intake of LHRH–SPIONs and SPIONs into breast cancer cells. Cells that had been incubated with two kinds of nanoparticles (15 nm LHRH–SPIONs and 15 nm SPIONs) for different time periods were fixed for 2–3 h with 2% glutaraldehyde in a 0.2 M sodium cacodylate buffer with a pH of 7.2. The cells were then washed a few times in a 0.2 M sodium cacodylate buffer (pH 7.2) in order to remove any residual nanoparticles that existed outside the cells.

After post-fixing on ice with a 1% OsO_4 in sodium veronal buffer for 1 h, the cell specimens were stained with 0.25% toluidine blue in 0.2 M sodium sacodylate buffer for another 60 min. They were then left overnight in the dark in 2% uranyl acetate in a 0.05 M sodium maleate buffer. Dehydration of the cell specimens was done by immersing them gradually in EtOH with increasing concentrations from 30% to 100%.

After dehydration, the cell specimens were embedded in epoxy resin. The resin was then allowed to polymerize overnight in an oven that was operated at 60 °C. TEM samples were prepared by cutting 60 nm thick sections from the resins using a Reichert Ultracut E Microtome (Reicher-Jung®). The thin slices were then mounted on standard hexagonal mesh copper grids for TEM observation, which was carried out in a LEO 912AB TEM (Zeiss, Thornwood, NY).

3.3.2. Spectrophotometry

Spectrophotometric analysis was used to study the intake of differently sized SPIONs and LHRH–SPIONs into breast cancer cells. This was done after the cells had been incubated with five kinds of nanoparticles (5 nm SPIONs, 10 nm SPIONs, 15 nm SPIONs, 30 nm SPIONs, and 15 nm LHRH–SPIONs) for different time periods. Subsequently, a spectrophotometric analysis technique was used to determine the concentration of these various nanoparticle types inside cells. This was achieved by measuring cell density with a standard Hemocytometer. The cells were then separated from the medium using a centrifuge (125 $\times g$ for 7 min).

The separated cells, as well as any nanoparticles that had been incorporated into them, were dissolved in 2.5 ml of 12 M HCl solution. This ionizes the Fe_3O_4 into iron cations that form highly colored complexes when reacted with the thiocyanate ion. The solution was then mixed with a 1.5 M potassium thiocyanate solution that turned red in color upon absorption of light with a wavelength of 447 nm. A Unico 1200 spectrophotometer (United Products & Instruments, Inc, Dayton, NJ) was used to measure the absorbance of each solution. The measured absorption was then converted into the concentration of iron cations in each solution. By considering the concentration of cells in each solution, the average mass of nanoparticles contained within each cell was estimated.

3.4. In-vivo experiments

Both TEM and MRI were used in the studies of breast cancer xenografts and metastases in the lungs of athymic nude mice. Tumors were induced by the injection of human breast cancer cells into the interscapular region, which were then allowed to grow for 30 days. During this period, tumors developed in the mice, and metastases occurred in the lungs [11]. LHRH–SPIONs were then injected into the lateral tail vein, and the mice were sacrificed after 20 h. Subsequently, the primary tumors and metastases in the lungs were preserved for the TEM and MRI experiments. All of the animal experiments were designed and conducted at the Pennington Biomedical Center of the Louisiana State University. They were in compliance with the institutional animal care and use committee and the principles of laboratory animal care of the National Institute of Health (NIH), USA. The following TEM and MRI studies were performed on these samples:

3.4.1. Transmission electron microscopy

The tumor tissues were fixed in glutaraldehyde (2.5% glutaraldehyde in 0.1 M sodium cacodylate with 2 mM $CaCl_2$, pH 7.3) and then cut into small pieces of ~1 mm [3], which were stained overnight using 1% uranyl acetate in the dark. The stained tissue specimens were dehydrated and embedded in resin using a method similar to that employed in the *in-vitro* TEM studies. Subsequently, the samples were cut into 60 nm foils and mounted on Cu mesh grids for TEM observation [19].

3.4.2. Magnetic resonance imaging

The magnetic resonance imaging experiments were conducted on a 7 T animal imager Magnex magnet, interfaced to a Bruker Biospect spectrometer. The MRI experiments involved the imaging of specimens that were excised from mice injected with LHRH–SPIONs or saline solution, before sacrificing the mice to extract the organs. The samples (approx. 1 cm × 1 cm × 1 cm) were placed in a specific plastic thin-wall box. To prevent the samples from drying, the tubes were

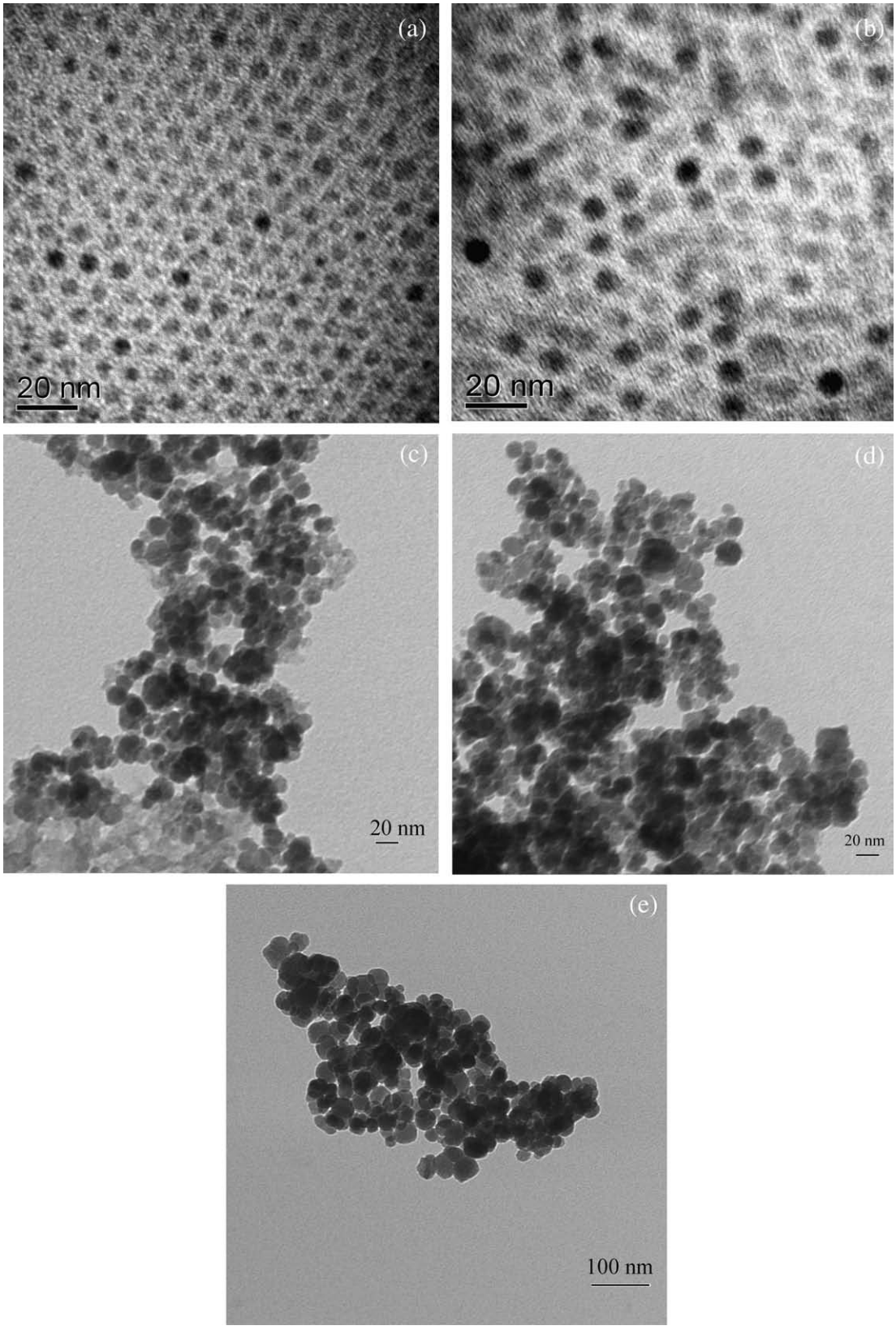

Fig. 2. TEM micrographs of SPIONs: (a) 5 nm SPIONs; (b) 10 nm SPIONs; (c) 15 nm SPIONs; (d) 15 nm LHRH–SPIONs; (e) 30 nm SPIONs.

filled with D_2O and the whole box was sealed with Parafilm. Standard T2 images of breast tissue were acquired using a FOV [6.5, 6.5] cm and a slice thickness of 2 mm.

T2 measurements were also acquired at room-temperature, on an excised tissue, before and after injection of LHRH–SPIONs. The RF sequence used for these T2 measurements was a standard spin-echo sequence: 90 — TE/2 — Crush Gradient Pulse (7 G/cm, 1 ms) — 180° — Crush Gradient Pulse (7 G/cm, 1 ms) — TE/2., where the echo time (TE) was varied. The echo intensity was then measured at different TE values and the T2 number was obtained by fitting the signal decay

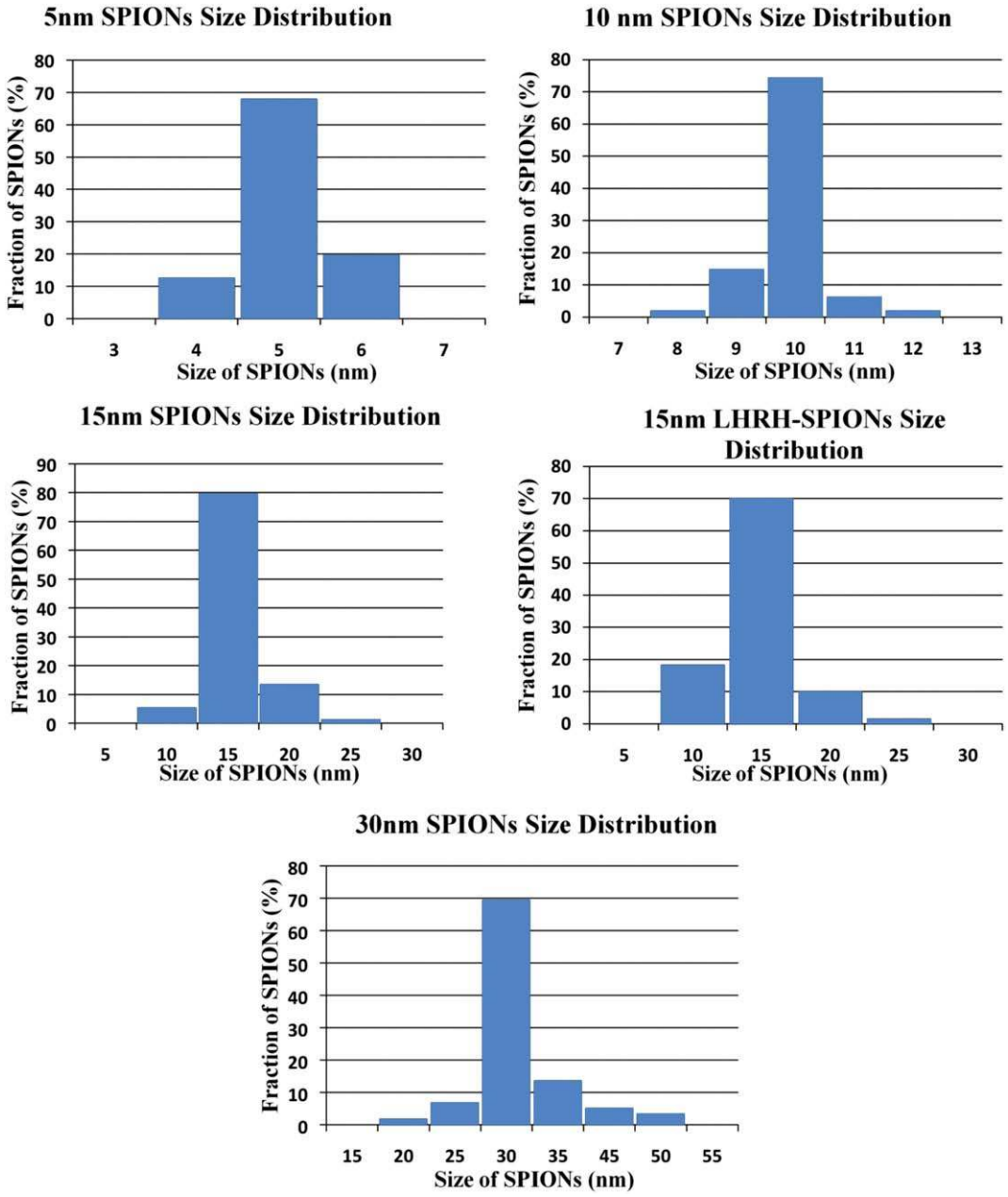

Fig. 3. Histogram plots of size distribution of five different SPIONs.

with a mono exponential curve exp{−TE/T2}. The multi-CRAZED experiments of lung samples (0.5 cm × 1 cm × 1 cm) were conducted on a 600-MHz Varian Unity^{plus}-Inova NMR spectrometer, following a similar procedure to that used by Shannon et al. [20].

Control MRI experiments were also performed on grapes to see if the contrast enhancement provided by injected nanoparticles could overcome tissue heterogeneity. Grapes were chosen for their inherent contrast and high water content. These grapes were injected with SPION nanoparticles before investigating them in the same 7T MRI system that was used in the tissue MRI experiments.

4. Results

4.1. Nanoparticle

TEM micrographs of the five different nanoparticle types used in this study are shown in Fig. 2, and the corresponding size distribution histograms are presented in Fig. 3. It is clear that the nanoparticles have roughly spherical morphologies with varying size dispersions. The nominal 5 and 10 nm SPION preparations have the tightest size distributions which facilitates their self-assembly into ordered hexagonal monolayer arrays upon solvent evaporation (Fig. 2(b) and (c)). The 15 nm and 30 nm SPION preparations on the other hand have a wider spread in their size distributions, which results in them having a tendency to form more irregular 3D aggregates upon drying (Fig. 2 (c), (d) and (e)). It is also interesting to note from Figs. 2(c), (d) and 3, that the 15 nm SPIONs and 15 nm LHRH–SPIONs have very similar distributions, which confirms that no significant size change resulted from incorporating the LHRH coating on the SPIONs.

4.2. In-vitro experiments

4.2.1. TEM results

TEM micrographs of cells incubated for different time durations with 15 nm SPIONs are presented in Fig. 4, while the corresponding images of cells incubated with 15 nm LHRH–SPIONs are shown in

Fig. 5. From the images, it is clear that the number of nanoparticles that accumulate inside cells increase as the incubation time increased. After ~180 min of incubation, the cell intake of LHRH–SPIONs was also far greater than that of SPIONs (shown in Figs. 4(c) and 5(c)). Since the two kinds of nanoparticle solutions have the same nanoparticle concentration, this increased intake of LHRH–SPIONs is attributed to the over-expression of LHRH receptors on the membranes of the breast cancer cells.

The observed nanoparticle interactions with cancer cell membranes are shown in Figs. 6 and 7. In the case of Fig. 6, the mechanism of nanoparticle entry is shown to be analogous to the endocytosis mechanism by which food particles enter cells. The cell/nanoparticle interactions generally result in the perturbation of the cell membrane (Fig. 6(b)), presumably as a result of the receptor-mediated endocytosis of nanoparticle clusters. The nanoparticle clusters are then encapsulated, as shown in Fig. 6(c). In this micrograph an encapsulated LHRH–SPION nanoparticle cluster can be observed that has just entered into the cell membrane from the surrounding environment.

The material transport mechanisms that are involved in the entry of the LHRH–SPION clusters are shown even more clearly in the TEM micrograph presented in Fig. 7. In addition to the nanoparticle-induced membrane perturbation, the image shows different stages of how the nanoparticle clusters are transported into the cancer cells. First, the evolving curvatures trap the nanoparticle clusters along the perimeter of the cell membrane. The clusters are then transported into the cytoplasm, as shown in Fig. 7(b). Most of the nanoparticle clusters remain in the cytoplasm, where their presence may be used to promote enhanced contrast in MRI imaging.

4.2.2. Spectrophotometric analyses

The measured uptake of SPION is presented in Fig. 8, in which the nanoparticle uptake per cell is plotted as a function of cell culture time. Most importantly the results show that the uptake of LHRH–SPIONs is greater than that of SPIONs alone. Also, the uptake of larger SPIONs is greater than that of smaller SPIONs, at least in the 5 to 30 nm particle size ranges. Furthermore, the initial rates of uptake are relatively fast, during the first 25 min of cell culture.

However, in the case of the 15 nm LHRH–SPIONs, the uptake reaches a plateau of ~1400 ng per cell after cell culture duration of ~25 min. A slight decrease in nanoparticle content is shown for the unconjugated 15 nm SPIONs, after reaching a peak value of ~800 ng per cell during the first 25 min of cell culture. When compared to 15 nm SPIONs, an increased level of nanoparticle content is noted for 30 nm SPIONs, after reaching a peak value of ~850 ng per cell during

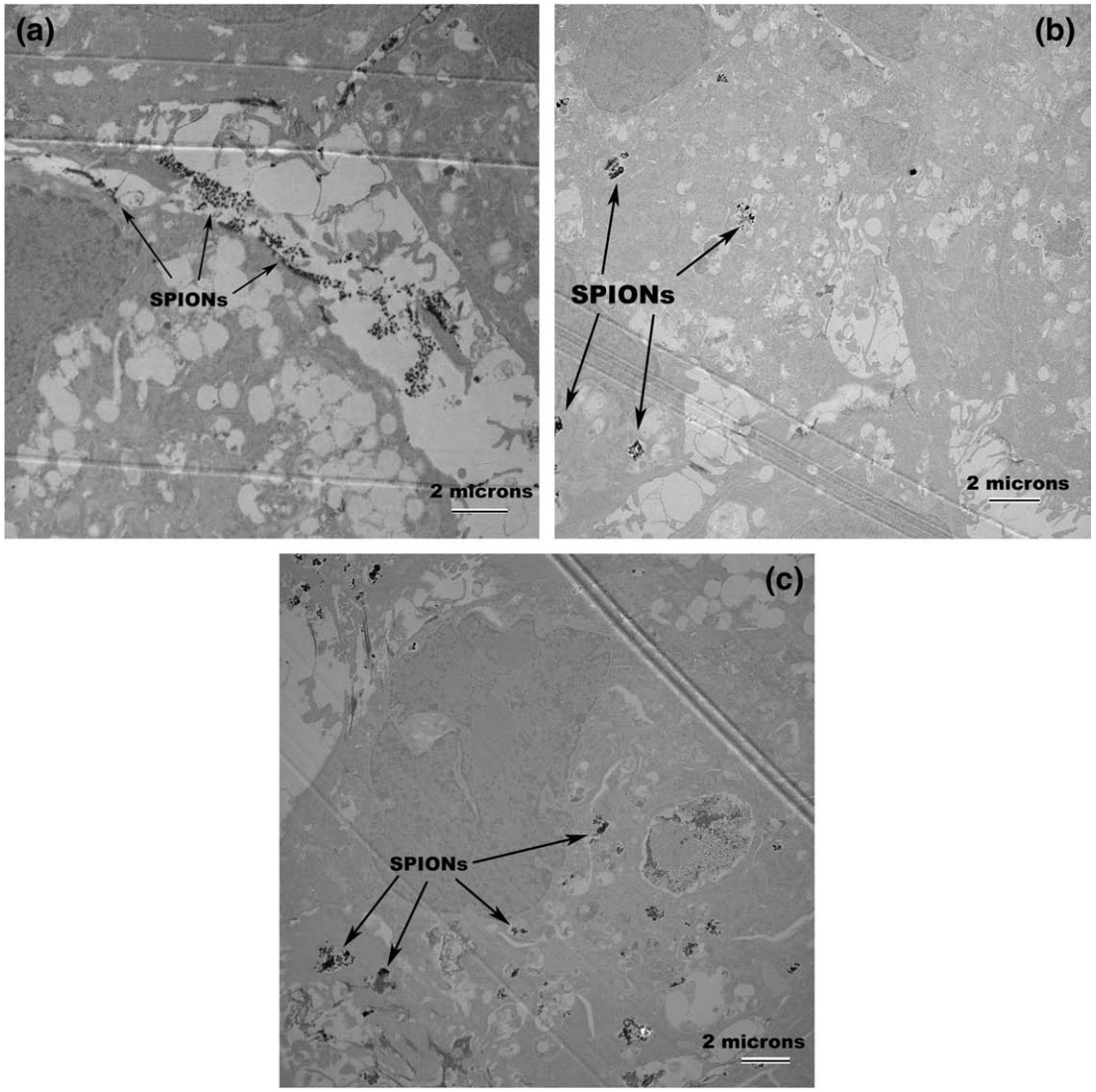

Fig. 4. TEM micrographs of breast cancer cells incubated with 15 nm SPIONs: (a) image of cell incubated with SPIONs for 10 min; (b) image of cell incubated with SPIONs for 60 min; (c) image of cell incubated with SPIONs for 180 min.

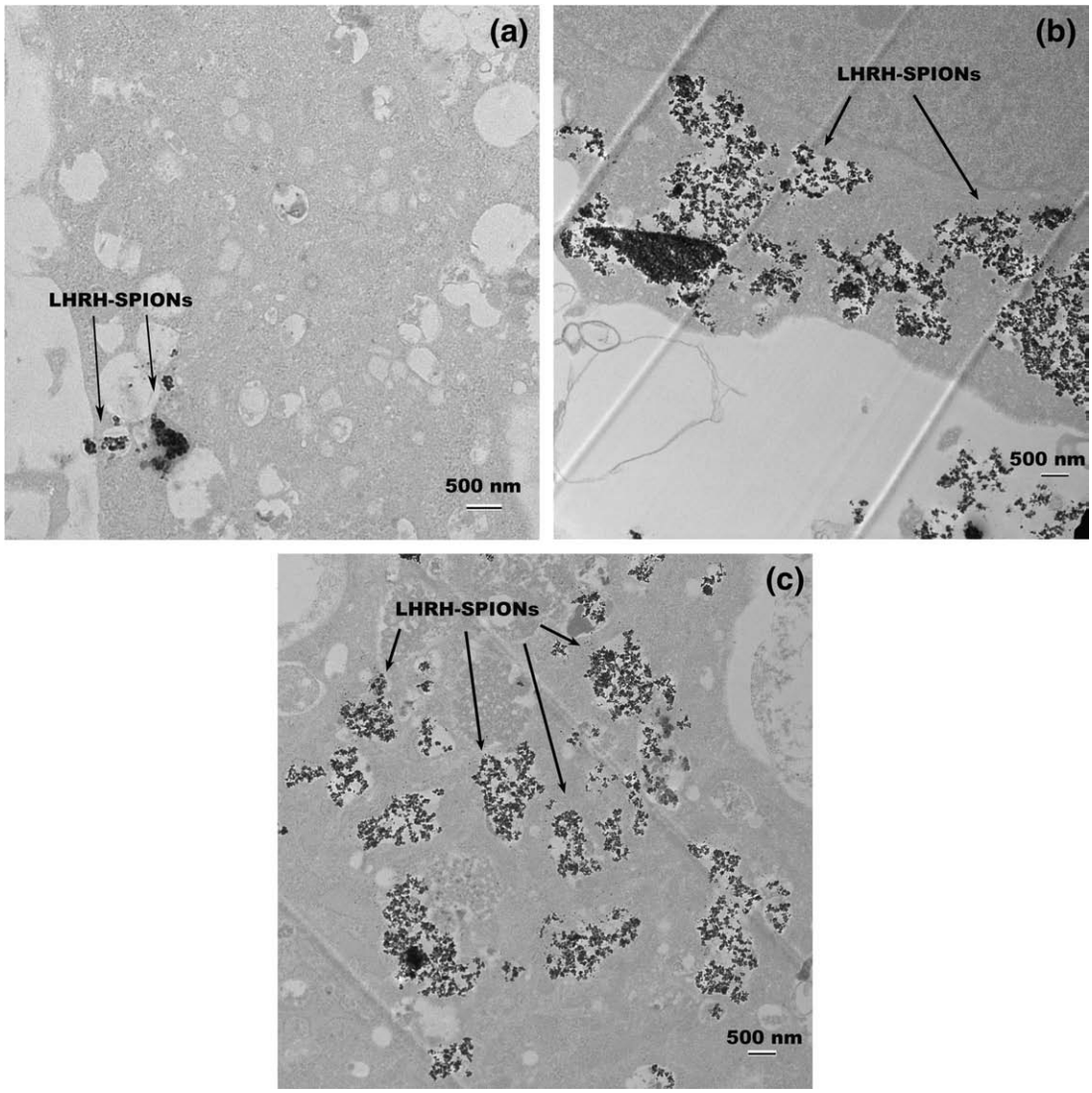

Fig. 5. TEM micrographs of breast cancer cells incubated with 15 nm LHRH–SPIONs: (a) image of cell incubated with LHRH–SPIONs for 15 min; (b) image of cell incubated with LHRH–SPIONs for 30 min; (c) image of cell incubated with LHRH–SPIONs for 180 min.

the first 25 min of cell culture. In contrast, a significantly lower level of nanoparticle content is found for 5 nm and 10 nm SPIONs, as shown.

Hence, the current *in-vitro* studies clearly show that the LHRH–SPIONs enter preferentially into breast cancer cells. The spectrophotometry results also show that the amount of LHRH–SPION uptake is about twice as much as that of the SPIONs that have not been functionalized with LHRH. *In-vivo* evidence of nanoparticle uptake will be presented in the next section along with T2 MRI images that show improvements in T2 contrast can be achieved by the injection of SPIONs and LHRH–SPIONs.

4.3. In-vivo experiments

4.3.1. Control experiments

The MRI imaging results obtained from the control experiments on grapes are presented in Fig. 9. The T2 contrast associated with the injected stream of nanoparticles can be distinguished clearly from the heterogeneous structure of the grape, as shown in the longitudinal section Fig. 9a. Also, the transverse cross-section of Fig. 9b reveals the presence of a dot labeled with the arrow in Fig. 9b corresponding to the effect of the injected nanoparticles on the local T2 contrast. The results from the control experiments, therefore, suggest that the local contrast enhancement is provided by the injected nanoparticles and overcome the heterogeneity of the grape structure.

4.3.2. T2 imaging of tumors

The T2 images obtained from the breast cancer xenografts from mice injected with LHRH–SPIONs are compared with those of tumor tissue without magnetic nanoparticles in Fig. 10. It is clear that Fig. 10 shows an enhancement in MRI contrast over a larger area, with the top set of image of the LHRH–SPION injected breast cancer tissue having a much greater contrast than the lower set of images from a virgin breast cancer xenograft without injected nanoparticles.

Furthermore, the average bulk T2 measurements on tumor tissues exhibit a decrease of ~10–15% in T2 number when the excited tissues are injected with nanoparticles. In particular, a T2 of 76 ms was found for the excised tumor tissue before injection. A T2 of 63 ms was found for the same tissue after the LHRH–SPION injection.

The results, therefore, suggest that classical T2 measurements may be used to provide evidence of the specific attachment of LHRH–SPIONs in tumor tissue. The specific attachment of LHRH–SPIONs is shown clearly in Fig. 11a in which LHRH–SPION clusters are revealed in the TEM image of tumor tissue from a female mouse injected with LHRH–SPIONs. The composition of the SPIONs has also been verified using energy

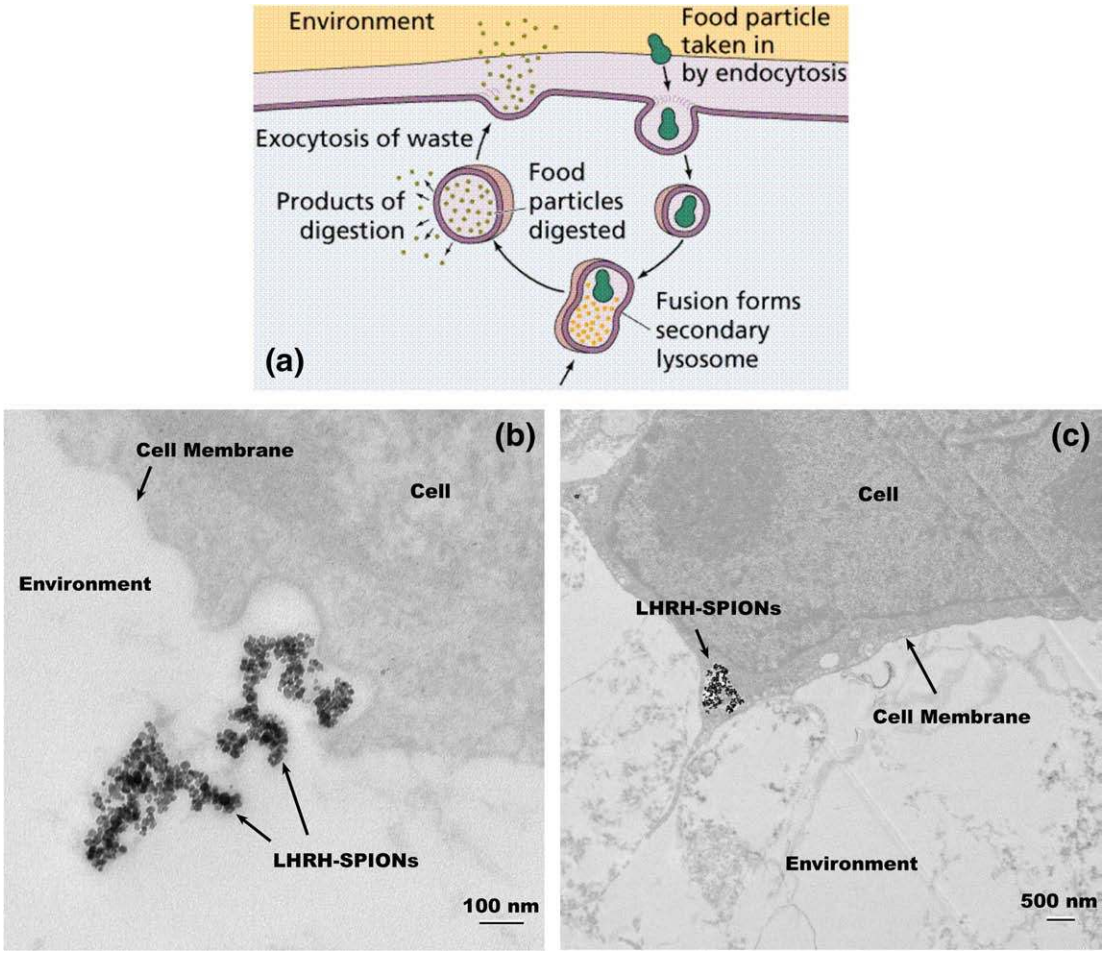

Fig. 6. Comparison of an endocytosis schematic diagram with TEM micrographs of breast cancer cells incubated with LHRH–SPIONs for 30 min(a) Schematic representation of Endocytosis (http://www.emc.maricopa.edu/faculty/farabee/BIOBK/endocytosis.gif). (b) Micrographs of nanoparticles LHRH–SPIONs that were about to enter cells with curved cell membrane. (c) Micrographs of encapsulated LHRH–SPIONs or SPIONs in the cytoplasm of a cancer cell.

dispersive X-ray spectroscopy (XEDS), as shown in Fig. 11b. Note that the Cu K_α and K_β peaks correspond to a fluorescence effect from the copper TEM grids, while the Fe K_α and K_β peaks are a signature of the Fe_3O_4 nanoparticles.

4.3.3. Multi-CRAZED imaging

A montage of multi-CRAZED images of the breast tumor specimens are presented in Fig. 12 [20]. These show that the incorporated LHRH–SPIONs enhance the contrast in multi-CRAZED magnetic anisotropy images of the

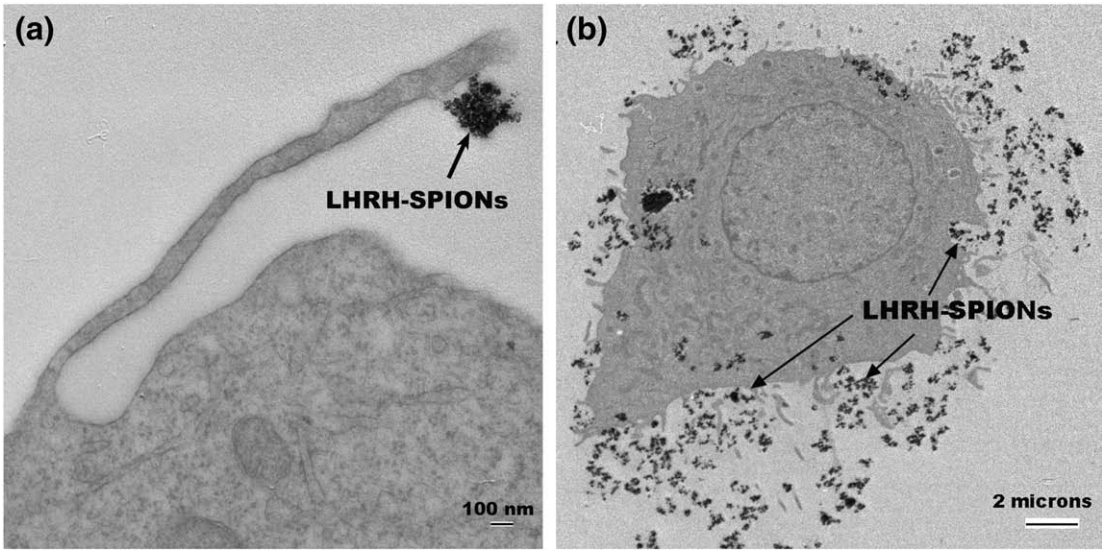

Fig. 7. TEM micrographs illustrating how LHRH–SPIONs are interacting with breast cancer cells: (a) Nanoparticle cluster interaction with cell membrane; (b) entry and transport of nanoparticle clusters within cytoplasm.

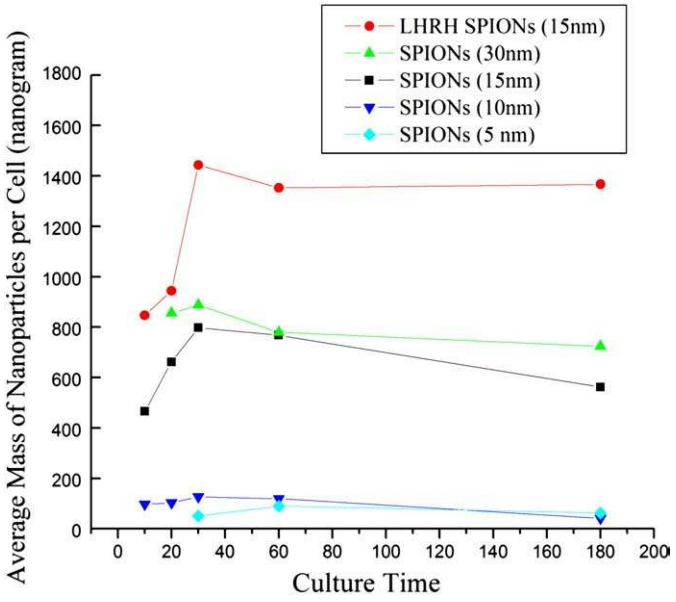

Fig. 8. Plot of average nanoparticle mass inside breast cancer cells against incubation time.

breast tumor specimens. The terms DQC, SQC, ZQC, -SQC and -DQC have already been defined in Section 2 and elsewhere [20]. In any case, the fact that multi-CRAZED images provide enhanced contrast should be of clinical significance.

Similarly, contrast enhancement was observed in the multi-CRAZED images of lung tissue in which metastases were observed (Fig. 13a–j). This is consistent with prior TEM observations of significant LHRH–SPION accumulation in the metastases in the lungs of tumor bearing mice [19]. Additional TEM micrographs of LHRH–SPIONs and SPIONs accumulated in the metastases in the lungs are presented in Fig. 14. Such high concentrations of contrast enhancement agents enable the increased contrast in the multi-CRAZED images of the metastatic lung tissue shown in Fig. 13f–j. Note that the concentration of SPIONs is much less in the absence of LHRH (Fig. 14b). Hence, the preliminary data suggests that LHRH enables the specific targeting of breast tumor (Fig. 11a) and metastatic lung tissue (Fig. 14a). Also, once attached, the LHRH–SPIONs provide valuable MRI contrast enhancement (Figs. 10, 12 and 13).

4.3.4. MRI and nanoparticle accumulation in tumor cells and peripheral organs

The body distribution of LHRH–SPIONs and SPIONs in tumor bearing mice is strongly dependent on the type of nanoparticles injected. Up to 60% of the injected LHRH–SPIONs accumulated in the tumors and lungs of tumor bearing mice, while 5% were recovered in the liver. In contrast, unconjugated SPIONs accumulated preferentially in the liver, and only 8% of the nanoparticles were found in breast tumor tissue [11,19,29]. It is also interesting to note here that the accumulated nanoparticles in the liver can also give rise to MRI contrast enhancement. In the case of bulk T2 measurements, this results in a change in T2 from 8 to 4 ms.

5. Modeling

5.1. Single particle model

Receptor-mediated endocytosis is one of the most important methods through which viruses and bio-materials enter cells [26,27]. However, the effects of nanoparticle size would affect their uptake into cells are still unclear. This stimulated Gao et al. [28] to theoretically analyze the factors that contribute to this size effect. In their model, they considered a cell membrane containing diffusive mobile receptors that wrap around individual spherical particles with compatible immobile and uniformly distributed surface ligands. Since the nanoparticle size ranges from a few nm to hundreds of nm, which is much smaller than the cell membrane dimensions (tens of microns), the cell membrane can be approximated to a flat membrane.

When the nanoparticle comes into contact with the initially flat membrane, the cell membrane starts to wrap around the particle, while the receptors on the cell membrane diffuse to the wrapping site and bind with the ligands on the particle surface, as shown in Fig. 15. In this process, the binding between ligands and receptors lowers the free energy of interaction at the cost of the elevated elastic energy associated with increased local curvature of the membrane, and the reduced configurational entropy associated with receptor immobilization.

The receptors on the cell membrane are assumed to be uniformly distributed with density ξ_0 before the nanoparticle comes into contact with the cell, and ξ_L is the ligand density on particle surface. Once nanoparticle contact occurs, the receptor density in the contact region is raised to the level of the ligand density, ξ_L, in the region surrounding the contact, the receptors are driven to the edge of the contact zone by

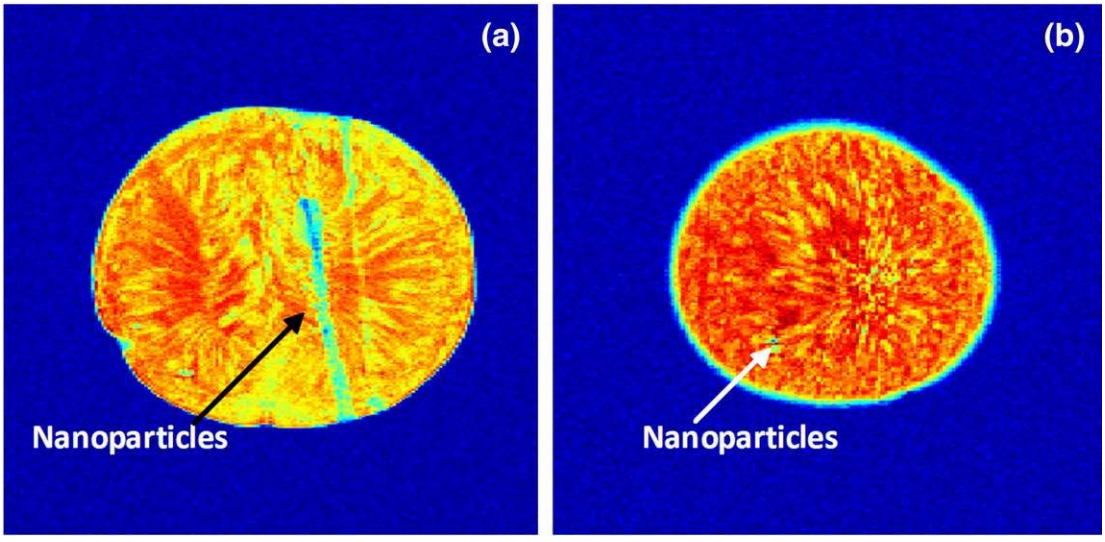

Fig. 9. MRI images of grape injected with a line of magnetic nanoparticles; (a) image of longitudinal cross section of the grape; (b) image of one transverse cross section of the grape.

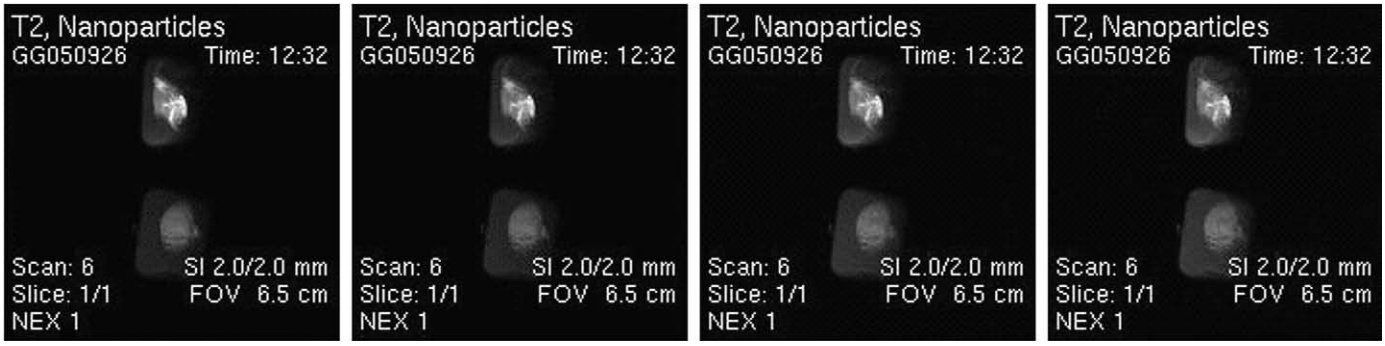

Fig. 10. T2 MRI images of breast tumor tissue. The top sample is the breast cancer xenograft from mice injected with LHRH–SPION, while the lower sample is the breast tumor tissue from saline control samples prepared without SPIONS.

diffusion, and the receptor density on other parts of the cell membrane can then be described as a distribution function $\xi(s,t)$. The free energy $F(t)$ is given by [28]:

$$F(t) = k_B T\left\{\int_0^{a(t)}\left(-\xi_L e_{RL} + \xi_L \ln\frac{\xi_L}{\xi_0} + \frac{1}{2}B\kappa_p^2\right)ds + \int_{a(t)}^{L}\xi\ln\frac{\xi}{\xi_0}ds\right\} \quad (1)$$

where k_B is the Boltzmann constant, T is the absolute temperature, $a(t)$ is the radius of the contact region, L is the membrane radius, and $k_B T e_{RL}$ is the energy of a single receptor–ligand bond. The parameters $k_B T \ln\frac{\xi_L}{\xi_0}$ and $k_B T \ln\frac{\xi}{\xi_0}$ are the free energy per receptor associated with the loss of configurational entropy of the bound receptors and free receptors, respectively, while the quantity $\frac{1}{2}Bk_B T\kappa_p^2$ is the elastic bending energy of the membrane wrapping around a sphere. The optimal size for nanoparticle entry arises from an interplay between kinetics and thermodynamics — wrapping small particles is thermodynamically costly (and hence slow) due to rapid increase in the elastic bending energy, while wrapping large particles is energetically more favorable but slow due to diffusive nature of the receptor transport.

5.2. Particle cluster model

Experimental studies have shown that nanoparticles can also enter cells as clusters of nanoparticles [19]. Since nanoparticle clusters may well change the overall surface energies, a new model is derived here to take into account the surface energy effects on cell uptake of nanoparticle clusters.

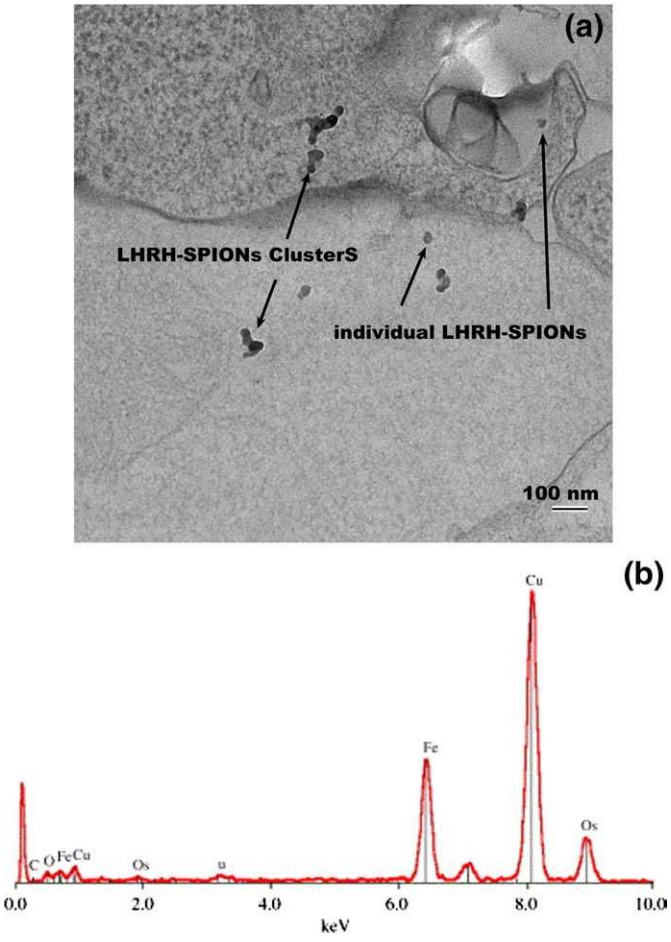

Fig. 11. (a) TEM micrographs of breast cancer cells from a female mouse injected with LHRH–SPIONs. Both individual particles and particle clusters distributed in the cell. (b). An XEDS spectrum collected from SPIONs distributed in tumor cells.

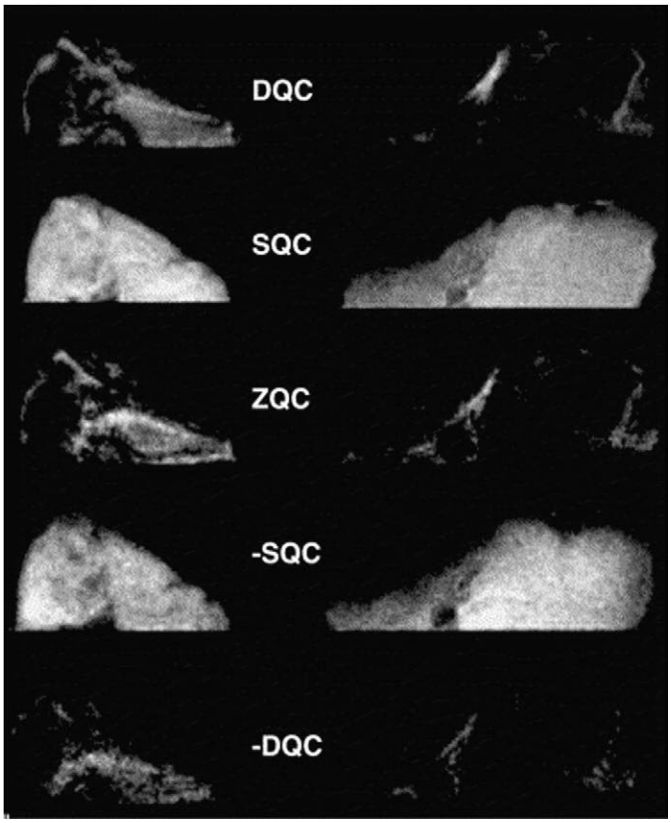

Fig. 12. Multi-CRAZED images of a mouse breast tumor embedded with 15 nm LHRH–SPIONs (left) and without nanoparticles (right). 0-quantum (ZQC image); 1-quantum (SQC image); 2-quantum (DQC image); −1-quantum (MSQC image); −2-quantum (MDQC image) (adapted from Ref. [20]).

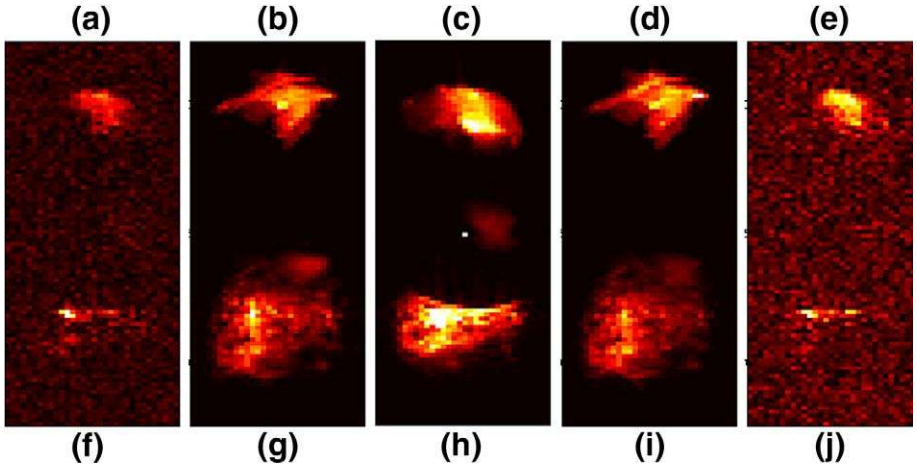

Fig. 13. Multi-Crazed MRI images of lung sections with metastases. The top row of images (a)–(e) are those without nanoparticles and the bottom row of images (f)–(j) are two small samples together: one with magnetic nanoparticles and one with LHRH conjugated magnetic nanoparticles. (a) and (f) are 0-quantum (ZQC image); (b) and (g) are 1-quantum (SQC) image; (c) and (h) are 2-quantum (DQC) image; (d) and (i) are −1-quantum (MSQC) image; (e) and (j) are −2-quantum (MDQC) image.

We still assume that the ligand density on the nanoparticles surface is ξ_L and the receptor density on the cell membrane is ξ_0 before the particle clusters come into contact with the cell membrane. Similarly, after the contact begins, receptors on the cell membrane will be driven to the contact region and the receptor density on other part of the cell membrane are described as a distribution function $\xi(s,t)$.

However, in addition to the free energy term defined in Eq. (1), an additional surface energy term must be included in the nanoparticle cluster model. We assume that the nanoparticles form close packed spherical clusters so every nanoparticle inside the cluster has 12 near-neighbor particles. Hence, each particle on the surface of the cluster has 6 near-neighbor particles, as in a face-centered cubic crystal structure. At the same time, considering the fact that the nanoparticles are mixed with cell culture medium (*in-vitro*) or body fluid (*in-vivo*), the surface energy between liquid and nanoparticles should also be considered. Suppose that the contact area between two nanoparticles is A_C and the surface energy between two nanoparticles is γ_1. We can also write the surface energy between the nanoparticle-cell culture medium and body fluid as γ_2 and the surface energy between nanoparticle cluster and cell membrane as γ_3. Then, assuming the nanoparticle radius is r and cluster radius is R, we can obtain the following surface energy terms:

$$U_{\text{surface}} = U_{\text{nanoparticle–nanoparticle}} + U_{\text{particle–medium}} + U_{\text{nanoparticle–cell membrane}} \tag{2}$$

$$U_{\text{nanoparticle–nanoparticle}} = \gamma_1 \times 12A_C \times \left(\frac{4\pi R^3/3}{4\pi r^3/3} - \frac{4\pi R^2}{\pi R^2}\right) + \gamma_1 \times 6A_C \times \frac{4\pi R^2}{\pi R^2} \tag{3}$$

$$U_{\text{nanoparticle–medium}} = \gamma_2 \times \left(4\pi r^2 - 12A_C\right) \times \left(\frac{4\pi R^3/3}{4\pi r^3/3} - \frac{4\pi R^2}{\pi R^2}\right) + \gamma_2 \times \left(4\pi R^2 - \int_0^{a(t)} ds\right) \tag{4}$$

$$U_{\text{nanoparticle–cell membrane}} = \gamma_3 \times \int_0^{a(t)} \mathrm{d}s. \tag{5}$$

By incorporating these additional surface energy terms into the free energy expression, we obtain the following expression for the free

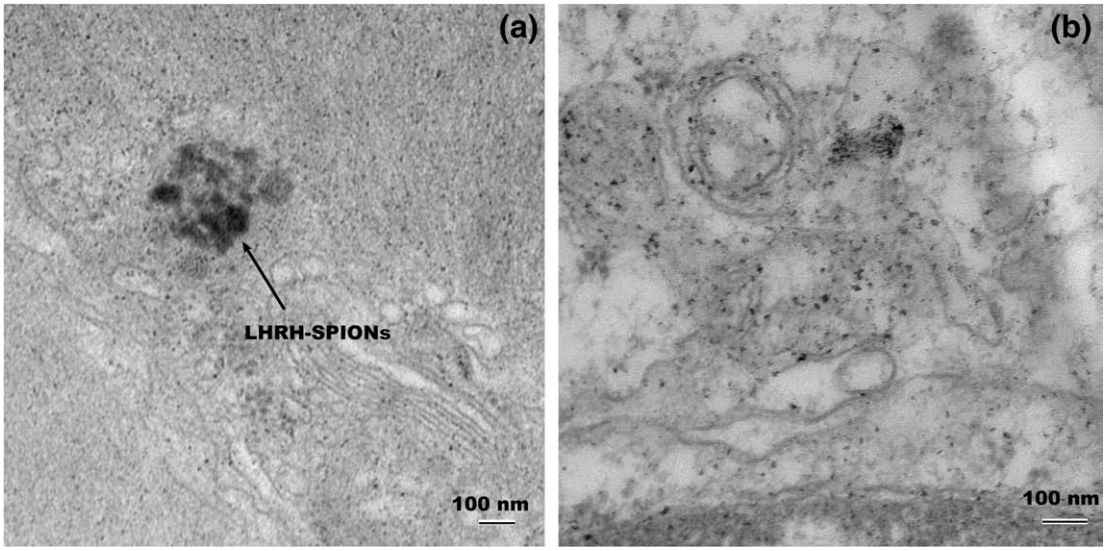

Fig. 14. TEM micrographs of LHRH–SPIONs and SPIONs accumulated in metastatic cells in lungs. (a) A significant amount of LHRH–SPION clusters in metastatic lung cells. (b) TEM micrograph of lung cell from a mouse injected with SPIONs. No SPIONs in lung cells.

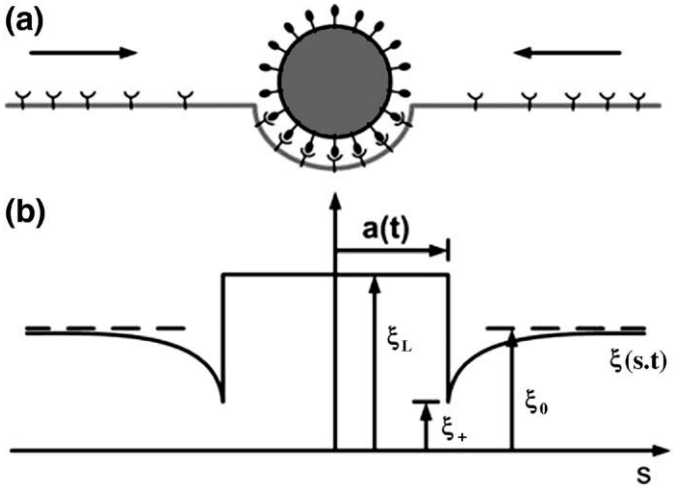

Fig. 15. Schematic illustration of the single particle interaction with cell membrane. (a) An initially flat membrane containing diffusive receptor molecules wraps around a ligand-coated particle. (b) The receptor density distribution in the membrane becomes nonuniform upon ligand–receptor binding; the receptor density is depleted in the near vicinity of the binding area and induces diffusion of receptors toward the binding site (adapted from Ref. [28]).

energy required for the nanoparticle cluster to enter the cell membrane:

$$F(t) = k_B T\left\{\int_0^{a(t)}\left(-\xi_L e_{RL} + \xi_L \ln\frac{\xi_L}{\xi_0} + \frac{1}{2}B\kappa_p^2\right)ds + \int_{a(t)}^{L}\xi\ln\frac{\xi}{\xi_0}ds\right\} + U_{\text{surface energy}}. \quad (6)$$

Since in Eqs. (3)–(5), some terms are time independent terms, such terms are not important to the wrapping dynamics. We will, therefore, consider these terms as constant in the wrapping process. Only the last term in Eqs. (4) and (5) contain time dependent term that can affect the wrapping dynamics. Hence, Eq. (6) can be simplified as:

$$\begin{aligned} F(t) = {} & k_B T\left\{\int_0^{a(t)}\left(-\xi_L e_{RL} + \xi_L \ln\frac{\xi_L}{\xi_0} + \frac{1}{2}B\kappa_p^2\right)ds + \int_{a(t)}^{L}\xi\ln\frac{\xi}{\xi_0}ds\right\} \\ & + \int_0^{a(t)}(\gamma_3 - \gamma_2)ds + \text{CONSTANT TERMS} = k_B T \\ & \times\left\{\int_0^{a(t)}\left(-\xi_L(e_{RL} + (\gamma_2 - \gamma_3)/\xi_L) + \xi_L\ln\frac{\xi_L}{\xi_0} + \frac{1}{2}B\kappa_p^2\right)ds + \int_{a(t)}^{L}\xi\ln\frac{\xi}{\xi_0}ds\right\} \\ & + \text{CONS. TERMS} \end{aligned} \quad (7)$$

The equation above clearly demonstrates that inclusion of the surface energy terms leads to a new, effective interaction energy between the ligand–receptor pairs, and thus affects wrapping dynamics. Further work needs to consider the dynamics on the process of nanoparticles forming cluster, which determines the optimal size of cluster to enter cells. In that case, the first few terms in Eqs. (4) and (3) will also be time dependent. However, this is beyond the scope of this paper.

5.3. Comparison of models and experiments

For a finite-sized membrane, it is not possible to obtain a closed-form analytical solution for ξ, the diffused receptor distribution. Hence, Gao et al. [28] solved this problem numerically. For a single nanoparticle entering a cell, the optimal particle radius for cell uptake is in the range of 27–30 nm, which is very consistent with our experimental results.

While for LHRH coated nanoparticles, the ligand density, ξ_L, on LHRH SPIONs is much greater than that for SPIONs. Hence, for LHRH–SPIONs, the first term in Eqs. (1) and (6), $k_B T\xi_L e_{RL}$, is much bigger than that obtained for SPIONs. This decreases the free energy of LHRH–SPIONs entering cells. Hence, the cell uptake of LHRH–SPIONs is greater than that of SPIONs. This is consistent with the spectroscopic data presented in Fig. 8.

To study the surface energy's effect, the difference between surface energy γ_2 and γ_3 are needed in our cluster model. These numbers are unknown. However, their approximate range can be estimated. Cell culture medium and body fluid are composed mainly of water, γ_2 can be estimated as the surface energy between SPIONs and water. The cell membrane also consists primarily of a thin layer of amphipathic phospholipids which have hydrophilic heads and hydrophobic tails. Since glycerol has a similar structure, we estimate that γ_3 should be comparable to the surface energy between glycerol and SPIONs.

Li and Logan [30] have studied the contact angle of water droplet on Fe_2O_3 surface and glycerol droplet on Fe_2O_3 surface. Based on their contact angle data, surface tension data of water and glycerol [31,32], we can calculate the surface energy between Fe_2O_3 and water, surface energy between Fe_2O_3 and glycerol through the Young Equation. Although SPIONs are Fe_3O_4 and not Fe_2O_3, we estimate that their surface energies are similar since both Fe_3O_4 surfaces and Fe_2O_3 surfaces are composed of iron and oxygen atoms. In this way, we estimate $(\gamma_2-\gamma_3)/\xi_L$ to be about 340 k_BT. From Eq. (7), we can also see this positive $(\gamma_2-\gamma_3)/\xi_L$ number significantly increases the thermodynamic driving force for particle clusters to enter cells. Hence, it is favorable for the cell uptake of nanoparticle clusters. This is consistent with our TEM observations (Figs. 4–7) in which several clusters were observed. Further work is clearly needed to measure the contact angle data on Fe_3O_4 surfaces.

With the exception of the surface energy terms, we used the same range of parameters and an approach described in Ref. [28] to study the nanoparticle clusters entering the cells. For a finite cell membrane with a size of 10 μm, the cluster model indicates that the cell can take in nanoparticle clusters with sizes up to ~500 nm. This is in good agreement with our TEM study as shown in Figs. 6(b) (c) and 7, which indicates that the cell can uptake nanoparticle clusters with cluster diameters as large as a few hundred nanometers.

Furthermore, the model predicts that analytically it takes around 5 min for a cell to take in spherical particle clusters with cluster diameter in the size range of ~300 nm. If we consider that the cell has finite size, the numerical solution predicts a little bit longer time but one that is still comparable to 5 min. Our TEM studies, as presented in Figs. 4(a) and 5(a), showed that after cells were incubated with nanoparticles for 10 or 15 min, the nanoparticle clusters had already entered the cells. Hence, the wrapping time predicted by the model is also consistent with our experimental results.

6. Discussion

The implications of the above results are quite significant. First, the results confirm our earlier hypothesis of using LHRH–SPIONs as specific contrast agents to provide sub-millimeter spatial resolution for the detection of breast cancer [11]. This could translate in practice into the detection of much earlier stages of cancer. Such early detection could therefore, potentially enhance the range of clinical options that are available to the patient for cancer treatment.

In addition, the cellular accumulation of the LHRH–SPIONs in tumors could enhance the localized treatment of breast cancer. This could enable clinical interventions by localized drug delivery [17,33–35] and hyperthermia [36,37] in ways that could result in a reduction of cancer mortality rates.

The general implications of the localized nature of the specific attachment of LHRH–SPIONs are also worthy of discussion. This targeted detection can in principle be combined with localized drug delivery in which cancer drugs are attached to LHRH–SPIONs. Such targeted drug delivery could facilitate the localized treatment of breast tumors, and could also significantly reduce the side effects of

currently used systemic applications of chemotherapy, since the drugs could be delivered in a highly targeted fashion, only to those sites that express the correct receptors.

Also, targeted drug delivery could require smaller volumes of cancer drugs to have a therapeutic effect. It is pertinent to mention that magnetically modulated drug delivery system utilizing LHRH–SPIONs are currently under development [17], and the concept of controlled release from nanosystems using oscillating magnetic fields has recently been demonstrated [38].

Furthermore, targeted drug delivery could be combined with hyperthermia (oscillating magnetic fields to induce local heating and the destruction of cancer cells) [39]. In such cases, the LHRH–SPIONs could provide an enhancement of the local magnetic fields that induce the heat due to the hysteresis in the induced deformation of the tumor tissue. A potential challenge for future work is in the development of cancer treatment strategies that utilize synergistic interactions between local hyperthermia and drug delivery.

7. Conclusions

This paper presents the results of *in-vivo* and *in-vitro* studies of the intake of LHRH–SPIONs and SPIONs into breast cancer cells. The results show how these nanoparticles enter and accumulate in the breast cancer cells as a function of particle size and exposure time. The uptake of the LHRH–SPIONs is also shown to be much greater than that of the unconjugated SPIONs in both *in-vitro* and *in-vivo* experiments. The increased uptake of intracellular accumulated LHRH–SPIONs is shown to provide T2 contrast enhancement that could lead to improved spatial resolution in MRI by classical T2 imaging. Such improved detection could be very significant for the early detection of cancer. Two models were discussed to study the mechanism of single nanoparticles and nanoparticle clusters entering cells. Primary results from the models are in good agreement with experimental results. However, further work is needed to get precise surface energy terms to improve the model. Furthermore, it is important to explore the use of LHRH–SPIONs in live mice (not just tissue) and larger animals. The potential conjugation of cancer treating drugs to LHRH–SPIONs also offers the potential for the design of specific targets that can be used to detect and destroy breast cancer.

Acknowledgements

The TEM work and the T2 MRI research were supported by the Division of Materials Research of the National Science Foundation (DMR 0231418). The multi-CRAZED MRI work was also supported by NIH grant EB 02122 and the State of New Jersey. The authors would also like to thank the Pennington Biomedical Center and the Center for Advanced Microstructures and Devices (CK and JH) for financial support of the cancer biology and nanoparticle synthesis work. Dr. Carola Leuschner thanks PBRC/LSU for support of the project "Detection of disseminated cells and micrometastases by ligand conjugated superparamagnetic iron oxide nanoparticles". Finally, the work at CAMD was supported financially by grants from NSF-EPSCoR ((2001–04) RII-03) and DARPA (Grant No: HR0011-04-C-0068). CJK and MPH would like to acknowledge the financial support of the NSF (Grant No. DMI-0304180 and Grant No. DMI-0457602) and the Pennsylvania Department of Community and Economic Development under contract # 20-906-0009. Prof Haataja would like to acknowledge support from NSF through NSF-DMR Grant No. 0449184 and the NSF-MRSEC Program, Grant No. DMR-0213706 at Princeton University.

References

[1] A. Jemal, T. Murray, E. Ward, A. Samuels, R.C. Tiwari, A. Ghafoor, E.J. Feuer, M.J. Thun, CA Cancer J. Clin. 55 (2005) 10–30.
[2] D.G. Gadien, NMR and its Applications to Living Systems, Oxford University Press, New York, 2000.
[3] A.E. Merbach, E. To'th, The Chemistry of Contrast Agents in Medical Magnetic Resonance Imaging, Wiley, Chichester, United Kingdom, 2001.
[4] P. Tartaj, M.P. Morales, S. Veintemillas-Verdaguer, T. González-Carreño, C. Serna, J. Phys. D: Appl. Phys. 36 (2003) R182–R197.
[5] R. Lawaczeck, H. Bauer, T. Frenzel, M. Hasegawa, Y. Ito, K. Kito, N. Miwa, H. Tsutsui, H. Vogler, H.J. Weinmann, Acta Radiol. 38 (1977) 584–597.
[6] S.G. Ruehm, C. Corot, P. Vogt, S. Kolb, J.F. Debatin, Circulation 103 (2001) 415–422.
[7] S.C.A. Michel, T.M. Keller, J.M. Frohlich, D. Fink, R. Caduff, B. Seifert, B. Marincek, R.A. Kubik-Huch, Radiology 225 (2002) 527–536.
[8] R.C. Semelka, T.K.G. Helmberger, Radiology 218 (2001) 27–38.
[9] W.S. Enochs, G. Harsh, F. Hochberg, R. Weissleder, J. Magn. Reson. Imaging 9 (1999) 228–232.
[10] G. Molema, D.K.F. Meijer, Drug Targeting, WILEY-VCH, 2001.
[11] C. Leuschner, C.S.S.R. Kumar, W. Hansel, J. Hormes, J. Biomed. Nanotechnol. 2 (2005) 229–233.
[12] C.S.S.R. Kumar, C. Leuschner, E.E. Doomes, L. Henry, M. Juban, J. Hormes, J. Nanosci. Nanotechnol. 4 (2004) 245–249.
[13] C. Leuschner, F. Enright, P. Melrose, W. Hansel, Prostate 46 (2) (2001) 116–125.
[14] B. Gawronska, C. Leuschner, F. Enright, W. Hansel, Gynecol. Oncol. 85 (2002) 45–52.
[15] C. Leuschner, F. Enright, B. Gawronska, W. Hansel, Breast Cancer Res. Treat. 78 (2003) 17–27.
[16] C. Leuschner, F. Enright, B. Gawronska, W. Hansel, Prostate 56 (4) (2003) 239–249.
[17] C.S.S.R. Kumar, C. Leuschner, J. Hormes, W. Hansel, Patent application No: 10/816,732, (2004).
[18] C. Leuschner, C.S.S.R. Kumar, J. Hormes, W. Hansel, Patent application Nos: 60/706,800 and 60/735,523, (2005).
[19] J. Zhou, C. Leuschner, C.S.S.R. Kumar, J.F. Hormes, W.O. Soboyejo, Biomaterials 27 (2006) 2001–2008.
[20] K.L. Shannon, R.T. Branca, G. Galiana, S. Cenzano, L.S. Bouchard, W.O. Soboyejo, W.S. Warren, Magn. Reson. Imaging 22 (2004) 1407–1412.
[21] W.S. Warren, http://www.princeton.edu/~wwarren/NMRintro.htm.
[22] W.S. Warren, W. Richter, A.H. Andreotti, S. Farmer, Science 262 (1993) 2005.
[23] Q. He, W. Richter, S. Vathyam, W.S. Warren, J. Chem. Phys. 98 (1993) 6779.
[24] S. Sun, H. Zeng, D.B. Robinson, S. Raoux, P.M. Rice, S.X. Wang, G. Li, J. Am. Chem. Soc. 126 (2004) 273.
[25] X. Teng, H. Yang, J. Mater. Chem. 14 (2004) 774.
[26] S.B. Sieczkarshi, G.R. Whittaker, J. Gen. Virol. 83 (2002) 1535–1545.
[27] L.B. Freund, Y. Lin, J. Mech. Phys. Solids 52 (2004) 2455–2472.
[28] H. Gao, W. Shi, L.B. Freund, PNAS 102 (27) (2005) 9469–9474.
[29] C. Leuschner, C.S.S.R. Kumar, W. Hansel, J. Zhou, W. Soboyejo, J. Hormes, Breast Cancer Res. Treat. 99 (2006) 163–176.
[30] B. Li, B.E. Logan, Colloids Surf., B Biointerfaces 36 (2004) 81–90.
[31] Carl L. Yaws, Chemical Properties Handbook, McGraw-Hill, Columbus, 1999.
[32] Surface Tension Values of Some Common Test Liquids for Surface Energy Analysis, http://www.surface-tension.de/.
[33] K.J. Widder, A.E. Senyei, D.G. Scarpelli, Proc. Soc. Exp. Biol. Med. 58 (1978) 141–146.
[34] A. Senyei, K. Widder, G. Czerlinski, J. Appl. Phys. 49 (6) (1978) 3578–3583.
[35] K. Mosbach, U. Shröder, FEBS Lett. 102 (1979) 112–116.
[36] J. Van Der Zee, Ann. Oncol. 13 (2002) 1173–1184.
[37] P. Wust, B. Hildebrandt, G. Screenivasa, B. Rau, J. Gellermann, H. Riess, R. Felix, P.M. Schlag, Lancet Oncol. 3 (2002) 487–497.
[38] Z. Lu, M.D. Prouty, Z. Gao, V.O. Golub, C.S.S.R. Kumar, Y.M. Lvov, Langmuir 21 (5) (2005) 2042–2050.
[39] R.K. Gilchrist, R. Medal, W.D. Shorey, R.C. Handelman, J.C. Parrott, C.B. Taylor, Ann. Surg. 146 (4) (1957) 596–606.